

Generalized modification in the lattice Bhatnagar-Gross-Krook model for incompressible Navier-Stokes equations and convection-diffusion equations

Xuguang Yang, Baochang Shi,^{*} and Zhenhua Chai

School of Mathematics and Statistics, Huazhong University of Science and Technology, Wuhan 430074, China

(Received 6 November 2013; revised manuscript received 19 May 2014; published 28 July 2014)

In this paper, two modified lattice Boltzmann Bhatnagar-Gross-Krook (LBGK) models for incompressible Navier-Stokes equations and convection-diffusion equations are proposed via the addition of correction terms in the evolution equations. Utilizing this modification, the value of the dimensionless relaxation time in the LBGK model can be kept in a proper range, and thus the stability of the LBGK model can be improved. Although some gradient operators are included in the correction terms, they can be computed efficiently using local computational schemes such that the present LBGK models still retain the intrinsic parallelism characteristic of the lattice Boltzmann method. Numerical studies of the steady Poiseuille flow and unsteady Womersley flow show that the modified LBGK model has a second-order convergence rate in space, and the compressibility effect in the common LBGK model can be eliminated. In addition, to test the stability of the present models, we also performed some simulations of the natural convection in a square cavity, and we found that the results agree well with those reported in the previous work, even at a very high Rayleigh number ($Ra = 10^{12}$).

DOI: [10.1103/PhysRevE.90.013309](https://doi.org/10.1103/PhysRevE.90.013309)

PACS number(s): 47.11.-j, 44.05.+e, 44.25.+f

I. INTRODUCTION

The lattice Boltzmann (LB) method, which first appeared in 1980s, has received increased attention in the study of various physical problems [1–3]. As a discrete kinetic numerical method, the LB method originates from a lattice gas automaton (LGA) [4], and it can also be derived from the continuous Boltzmann equation [5,6]. Due to its simplicity, the lattice Boltzmann Bhatnagar-Gross-Krook (LBGK) model, one of the most popular models in the LB method, has been widely used to study complex fluid flows. Actually, the original LBGK model is a solver for compressible Navier-Stokes equations in the incompressible limit. For this reason, when the original LBGK model is adopted to simulate incompressible fluid flows, it may lead to some errors in numerical results due to the compressibility effect. To eliminate this effect, the LBGK model has been improved by some researchers [7,8]. On the other hand, mass and heat transfer are usually coupled with fluid flow, and then the convection-diffusion equations are needed to describe the process of mass and heat transfer. In recent years, several LBGK models for convection-diffusion equations have been developed [9–16]. However, these available LBGK models for Navier-Stokes equations or convection-diffusion equations have a major deficiency: the numerical stability is strongly dependent on the dimensionless relaxation time τ , which is related to the fluid viscosity or the diffusion coefficient. If the value of τ is too large or too small (close to 0.5), the LBGK model would be unstable, which restricts the applications of the model in the study of complex fluid flows, such as non-Newtonian fluid flows, turbulent flows, problems such as multiphysics fields, and so on. For non-Newtonian fluid flows, the dimensionless relaxation time is related to the local viscosity, which is a function of the shear stress and varies at each time step. Therefore, the LBGK model may suffer numerical instability

when the shear stress rate approaches zero. For problems such as multiphysics fields, as with fluid flows in microchannels with heat or mass transfer, the Schmidt (Sc) or Prandtl (Pr) number is usually very high, which may cause the LBGK model to be unstable. In addition, for natural convection in a square cavity, which is a classic heat transfer problem (although in the framework of the LBGK model), there are many works available on this problem [17–20]. However, the results at high Rayleigh numbers (Ra) are rarely reported, which may be due to the instability of the LBGK model at a high Ra .

To overcome the above-mentioned deficiency of the LBGK model, many improvements have been made in recent years. With regard to the stability problem of the LBGK model for fluid flows, Qian *et al.* [21] presented a fractional propagation (FP) LB method (FPLBM), while McNamara *et al.* [22] proposed a Lax-Wendroff (LW) LB method (LWLBM). Based on these works, Guo *et al.* [23] further developed a general propagation LBGK scheme, and FPLBM and LWLBM can be regarded as its special cases. The above LB models were developed based on the discrete Boltzmann equation, and they utilize different discrete schemes to make the Courant-Friedrichs-Lewy (CFL) number smaller than 1. Therefore, the numerical stability can be improved. However, the propagation step is complicated and the rate of convergence is slowed down. While studying the LBGK model for convection-diffusion equations, Xiang *et al.* [24] introduced a parameter β in the second-order moment condition, such that the dimensionless relaxation time τ cannot be close to 0.5 through adjusting the parameter β . Although the stability of the LBGK model can be improved using this approach, the improvement is not significant. Inamuro [25] proposed a lattice kinetic scheme (LKS) for incompressible fluid flow with heat transfer. In his scheme, through adding a stress-tensor-related term in the equilibrium distribution function, a relaxation parameter of the stress tensor is introduced to make the dimensionless relaxation time τ be unity, hence the stability of the LBGK model can be improved. This idea has also been extended to the LBGK models for liquid-vapor multiphase flows [26]

^{*}Author to whom all correspondence should be addressed: shibc@hust.edu.cn

and non-Newtonian fluid flows [27]. However, we would like to point out that the scheme for incompressible fluid flows does not satisfy mass conservation law, and furthermore, the parallel characteristic of the LB method is also destroyed since the stress tensor in the added term is calculated using a finite-difference scheme.

In this work, a generalized modification, which can be considered as an improvement to the LKS [25], is proposed to improve the stability of the LBGK model. Similar to Ref. [25], a correction term is introduced to keep the dimensionless relaxation time in a proper range. As discussed in Refs. [25,28], the correction term in the modified LBGK model for the Navier-Stokes equations can be regarded as a discretization of viscous stress, and similarly, the correction term in the modified LBGK model for convection-diffusion equations can be considered as a discretization of the heat or mass flux. However, unlike the LKS proposed in Ref. [25], the role of the correction term is to keep the dimensionless relaxation time varied in a proper range rather than unity in simulating complex fluid flows. In addition, based on Chapman-Enskog analysis, the correction term added in the evolution equation as a force or source term is more reasonable than that in the equilibrium distribution function. Finally, in the present model, mass conservation law is satisfied and the calculation of the gradient operator in the correction term can be implemented locally, which retains the parallel characteristic of the LB method. For this reason, the following simulations are performed on a graphic processing unit (GPU), and a high computational efficiency can be obtained.

The rest of the paper is organized as follows. In Sec. II, the modified LBGK models for incompressible Navier-Stokes equations and convection-diffusion equations are presented. In Sec. III, several numerical experiments, including steady Poiseuille flow, unsteady Womersley flow, and natural convection in a square cavity, are conducted to test the accuracy and stability of the modified LBGK model, and finally some conclusions are summarized in Sec. IV.

II. THE MODIFIED LBGK MODELS

In this section, we will present two modified LBGK models for incompressible Navier-Stokes equations and the convection-diffusion equation:

$$\nabla \cdot \mathbf{u} = \mathbf{0}, \quad (1a)$$

$$\frac{\partial \mathbf{u}}{\partial t} + \nabla \cdot \mathbf{u}\mathbf{u} = -\nabla P + \nabla \cdot \nu \nabla \mathbf{u} + \mathbf{a}, \quad (1b)$$

$$\frac{\partial \phi}{\partial t} + \nabla \cdot \mathbf{u}\phi = \nabla \cdot D \nabla \phi, \quad (2)$$

where \mathbf{u} is the velocity, P is the pressure, ν is the kinematic viscosity, \mathbf{a} is the acceleration due to external force, ϕ represents a scalar variable, which can be substituted by temperature or concentration, and D is the diffusion coefficient.

A. The modified LBGK model for incompressible Navier-Stokes equations

The evolution equation of the modified LBGK model for incompressible Navier-Stokes equations is given as

$$\begin{aligned} f_i(\mathbf{x} + \mathbf{c}_i \Delta t, t + \Delta t) \\ = f_i(\mathbf{x}, t) - \frac{1}{\tau} [f_i(\mathbf{x}, t) - f_i^{\text{eq}}(\mathbf{x}, t)] + \Delta t S_i(\mathbf{x}, t), \end{aligned} \quad (3)$$

where τ is the dimensionless relaxation time, $f_i(\mathbf{x}, t)$ is the distribution function of a particle moving with velocity \mathbf{c}_i at position \mathbf{x} and time t , $S_i(\mathbf{x}, t)$ is defined as

$$\begin{aligned} S_i(\mathbf{x}, t) = \omega_i \frac{A[\nabla \mathbf{u} + (\nabla \mathbf{u})^T] : (\mathbf{c}_i \mathbf{c}_i - c_s^2 \mathbf{I})}{2\tau c_s^2} \\ + \left(1 - \frac{1}{2\tau}\right) F_i(\mathbf{x}, t), \end{aligned} \quad (4)$$

where the first term on the right-hand side of the above equation is the correction term, and A is a tunable parameter. $F_i(\mathbf{x}, t)$ is the discrete forcing term accounting for the external force, and it is given by [29]

$$F_i(\mathbf{x}, t) = \omega_i \left(\frac{\mathbf{c}_i \cdot \mathbf{a}}{c_s^2} + \frac{(\mathbf{a}\mathbf{u} + \mathbf{u}\mathbf{a}) : (\mathbf{c}_i \mathbf{c}_i - c_s^2 \mathbf{I})}{2c_s^4} \right). \quad (5)$$

$f_i^{\text{eq}}(\mathbf{x}, t)$ is the local equilibrium distribution function, and it is defined as [18]

$$f_i^{\text{eq}}(\mathbf{x}, t) = \lambda_i p + \omega_i \left[\frac{\mathbf{c}_i \cdot \mathbf{u}}{c_s^2} + \frac{\mathbf{u}\mathbf{u} : (\mathbf{c}_i \mathbf{c}_i - c_s^2 \mathbf{I})}{2c_s^4} \right], \quad (6)$$

where $\lambda_0 = (\omega_0 - 1)/c_s^2 + \rho_0/p$, $\lambda_i = \omega_i/c_s^2$ ($i \neq 0$), and c_s is the sound speed. The velocity and pressure of fluid flow are computed by

$$\mathbf{u} = \sum_i \mathbf{c}_i f_i + \frac{\Delta t}{2} \mathbf{a}, \quad (7)$$

$$p = \frac{c_s^2}{1 - \omega_0} \left(\sum_{i \neq 0} f_i - \omega_0 \frac{|\mathbf{u}|^2}{2c_s^2} \right). \quad (8)$$

For the two-dimensional case considered here, the two-dimensional-nine-velocity (D2Q9) LBGK model is usually used, and the discrete velocity \mathbf{c}_i in the D2Q9 model is defined as

$$\mathbf{c}_i = \begin{cases} (0,0)c, & i = 0, \\ (\cos[(i-1)\pi/2], \sin[(i-1)\pi/2])c, & i = 1,2,3,4, \\ 2(\cos[(i-5)\pi/2 + \pi/4], \sin[(i-5)\pi/2 + \pi/4])c, & i = 5,6,7,8, \end{cases} \quad (9)$$

where $c = \Delta x/\Delta t$ is the particle velocity, Δx and Δt are the lattice spacing and time step, respectively, and $c_s = c/\sqrt{3}$. The weight coefficients ω_i in the local equilibrium function are $\omega_0 = 4/9$, $\omega_i = 1/9$ ($i = 1-4$), $\omega_i = 1/36$ ($i = 5-8$).

Through Chapman-Enskog analysis, the incompressible Navier-Stokes equations can be recovered with $\nu = c_s^2(\tau - 1/2 - A)\Delta t$ (the detailed derivation process is given in the Appendix). For a fixed viscosity, it is clear that the dimensionless relaxation time τ can be varied in a proper range through tuning the parameter A . In addition, it should be noted that the strain rate tensor \mathbf{S} , which is included in the correction term $S_i(\mathbf{x}, t)$, can be computed locally in the LB method [30],

$$\mathbf{S} = \frac{\nabla \mathbf{u} + (\nabla \mathbf{u})^T}{2} = \frac{1}{2c_s^2 \Delta t (A - \tau)} \times \left(\sum_i \mathbf{c}_i \mathbf{c}_i (f_i - f_i^{\text{eq}}) + \Delta t (\mathbf{a}\mathbf{u} + \mathbf{u}\mathbf{a}) \right). \quad (10)$$

However, in the following simulations of natural convection in a square cavity, $\Delta t(\mathbf{a}\mathbf{u} + \mathbf{u}\mathbf{a})$ can be neglected due to the Boussinesq approximation.

B. The modified LBGK model for the convection-diffusion equation

The evolution equation of the modified LBGK model for the convection-diffusion equation reads

$$g_i(\mathbf{x} + \mathbf{c}_i \Delta t, t + \Delta t) = g_i(\mathbf{x}, t) - \frac{1}{\tau_\phi} [g_i(\mathbf{x}, t) - g_i^{\text{eq}}(\mathbf{x}, t)] + \Delta t \bar{S}_i(\mathbf{x}, t), \quad (11)$$

where τ_ϕ is the dimensionless relaxation time, and $\bar{S}_i(\mathbf{x}, t)$ is defined as

$$\bar{S}_i(\mathbf{x}, t) = \tilde{\omega}_i \frac{\mathbf{c}_i \cdot B \nabla \phi}{\tau_\phi} + \left(1 - \frac{1}{2\tau_\phi}\right) \bar{F}_i(\mathbf{x}, t), \quad (12)$$

where the first term on the right-hand side of the above equation is also a correction term and B is a tunable parameter. $\bar{F}_i(\mathbf{x}, t)$ is defined as

$$\bar{F}_i(\mathbf{x}, t) = \left(1 - \frac{1}{2\tau_\phi}\right) \frac{\mathbf{c}_i \cdot \phi \mathbf{a}}{c_s^2}. \quad (13)$$

$g_i^{\text{eq}}(\mathbf{x}, t)$ is given by

$$g_i^{\text{eq}}(\mathbf{x}, t) = \tilde{\omega}_i \phi \left[1 + \frac{\mathbf{c}_i \cdot \mathbf{u}}{c_s^2} + \lambda \frac{\mathbf{u}\mathbf{u} : (\mathbf{c}_i \mathbf{c}_i - c_s^2 \mathbf{I})}{2c_s^4} \right], \quad (14)$$

where λ is a constant, which can be taken as 0 or 1. The macroscopic quantity ϕ is calculated by

$$\phi = \sum_i g_i. \quad (15)$$

Equation (2) can also be recovered with $D = c_s^2(\tau_\phi - 1/2 - B)\Delta t$. In addition, through Chapman-Enskog analysis, it is easy to find that the gradient term $\nabla \phi$ can be calculated locally by

$$\nabla \phi = \frac{1}{c_s^2 \Delta t (B - \tau_\phi)} \left(\sum_i \mathbf{c}_i (g_i - g_i^{\text{eq}}) + \frac{\Delta t}{2} \phi \mathbf{a} \right). \quad (16)$$

Similarly to above discussion, the term $\Delta t \phi \mathbf{a}/2$ can also be neglected in the study of natural convection in a square cavity.

Remark 1. From Chapman-Enskog analysis, it can be observed that $f_i^{(0)}(\mathbf{x}, t) = f_i^{\text{eq}}(\mathbf{x}, t)$ at the zeroth-order in ε . If the correction term, which includes a gradient operator, is put in the equilibrium distribution function, the above equation cannot be satisfied because the gradient operator appeared as the first-order term in ε . On the other hand, the correction terms in Eqs. (4) and (12) can be viewed as discretizations of the viscous stress and heat or mass flux, and thus it seems more reasonable that the correction terms are treated as an external force or a source term.

Remark 2. The modification presented in this work can be extended to other LBGK models, such as the widely used DdQq model [31], in which the correction term $S_i(\mathbf{x}, t)$ should read

$$S_i(\mathbf{x}, t) = \omega_i \frac{A \rho [\nabla \mathbf{u} + (\nabla \mathbf{u})^T] : (\mathbf{c}_i \mathbf{c}_i - c_s^2 \mathbf{I})}{2\tau c_s^2} + \left(1 - \frac{1}{2\tau}\right) \rho F_i(\mathbf{x}, t). \quad (17)$$

III. RESULTS AND DISCUSSION

In this section, to test the accuracy and stability of the modified LBGK model, the steady Poiseuille flow, the unsteady Womersley flow, and the natural convection in a square cavity with a high Ra are studied. The nonequilibrium extrapolation scheme proposed in [32] is applied for the boundary conditions.

A. Steady Poiseuille flow

We first use the modified LBGK model to investigate the steady Poiseuille flow in a plane channel, which is defined in the region $0 \leq x \leq 2$ and $0 \leq y \leq 1$, and driven by a constant pressure gradient. In the following simulations, the initial and boundary conditions are set as follows:

$$\begin{aligned} u(x, y, 0) = v(x, y, 0) = 0, \quad p(x, y, 0) = p_0, \\ u(x, 0, t) = u(x, 1, t) = v(x, 0, t) = v(x, 1, t) = 0, \\ p(0, y, t) = p_{\text{in}}, \quad p(2, y, t) = p_{\text{out}}, \end{aligned} \quad (18)$$

where $p_0 = (p_{\text{in}} + p_{\text{out}})/2$, p_{in} and p_{out} are the pressure at the inlet and outlet, and they are set to be 1.1 and 1.0, respectively. Analytical solution for the Poiseuille flow is given by

$$u(y) = \frac{G}{\nu} \frac{L^2}{2} \left(\frac{y}{L} - \frac{y^2}{L^2} \right), \quad (19)$$

where $L = 2$ is the channel width, ν is the fluid kinematic viscosity, and $G = -\partial p / \partial x$ is the pressure gradient.

In our simulations, the Reynolds number is defined as $\text{Re} = Lu_{\text{max}}/\nu$, where $u_{\text{max}} = L^2 G / 8\nu$ is the maximum velocity along the center line of the channel; a grid size of 16×32 is used, and the dimensionless relaxation time τ is fixed to 1.0. Thus the variation of Re can be realized by changing the parameter A . To ensure that the numerical results are in a steady state, the following convergence criterion is used:

$$\sum_i \frac{|\mathbf{u}(\mathbf{x}_i, t + 1) - \mathbf{u}(\mathbf{x}_i, t)|}{|\mathbf{u}(\mathbf{x}_i, t + 1)|} \leq 10^{-10}. \quad (20)$$

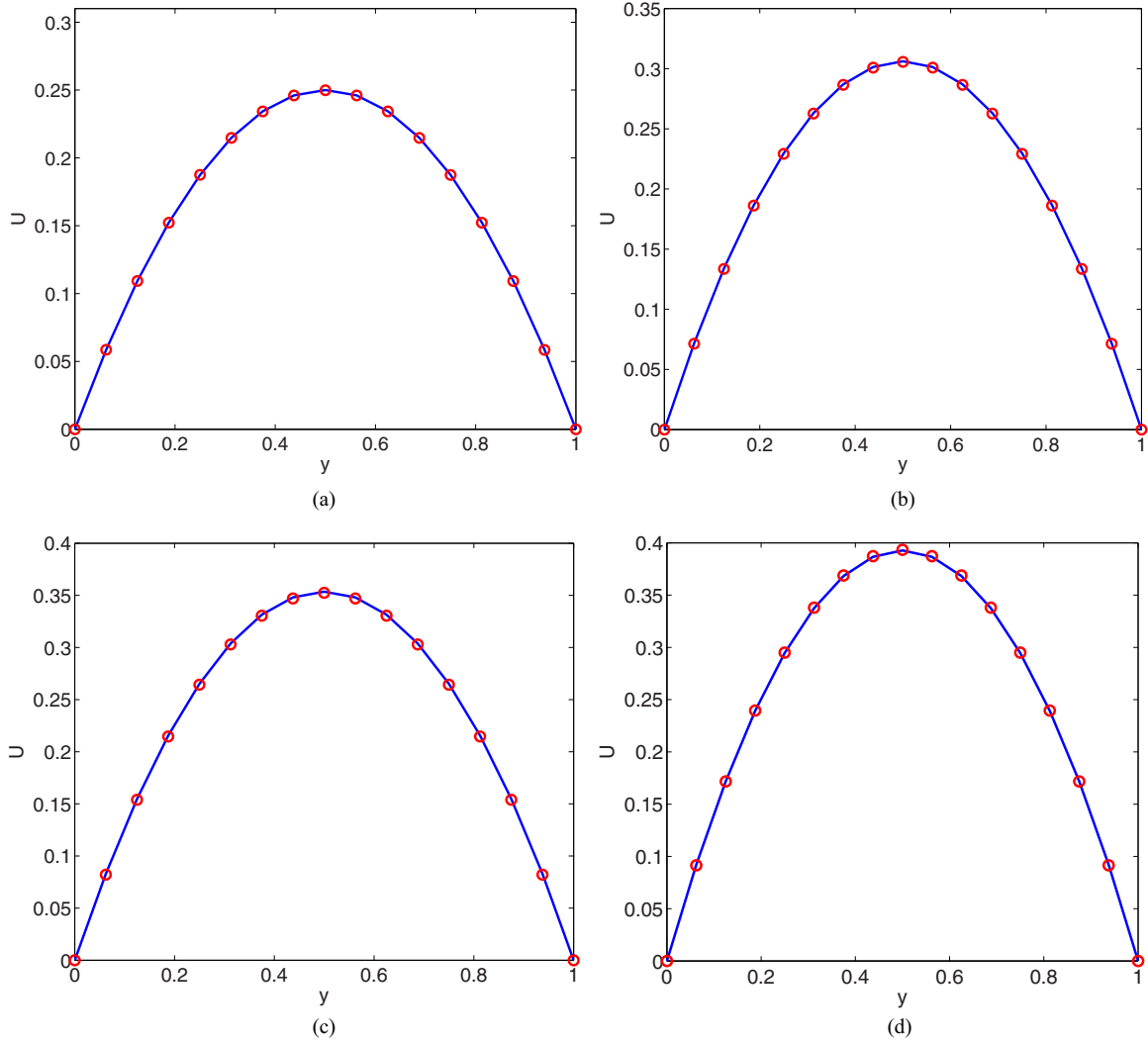


FIG. 1. (Color online) Comparisons between numerical results and analytical solutions of velocities at different Re numbers: (a) Re = 10, A = 0.02; (b) Re = 15, A = 0.04; (c) Re = 20, A = 0.06; (d) Re = 25, A = 0.08. Solid line: analytical solutions; circle: numerical solutions.

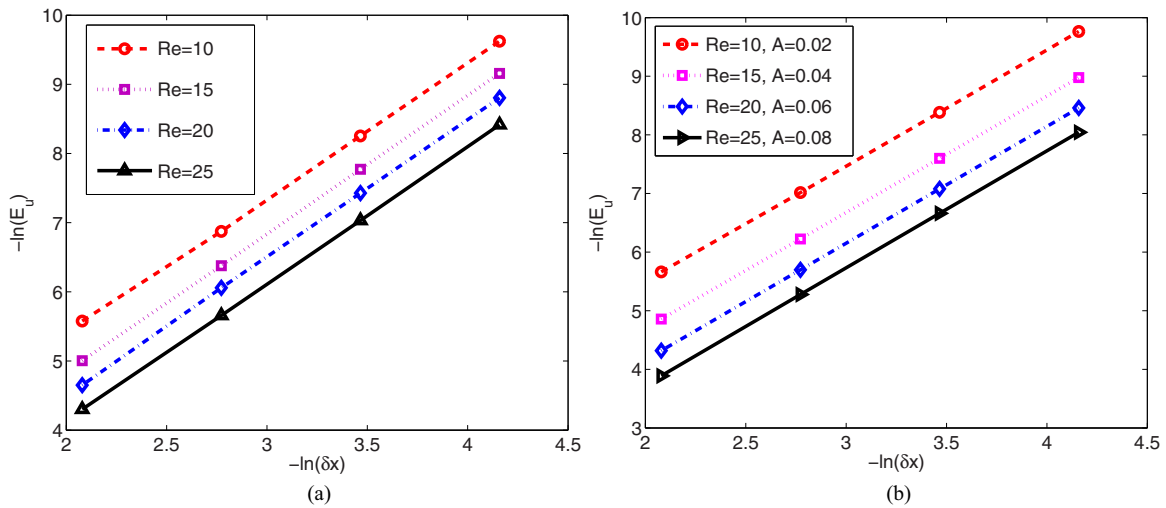


FIG. 2. (Color online) GRE at different lattice spacings and Re numbers: (a) nonmodified LBGK model, (b) modified LBGK model.

TABLE I. GRE by the nonmodified LBGK model with different Re numbers and different lattice spacings.

Re	E_u			
	$\delta x = 1/8$	$\delta x = 1/16$	$\delta x = 1/32$	$\delta x = 1/64$
Re = 10	3.785×10^{-3}	1.035×10^{-3}	2.601×10^{-4}	6.613×10^{-5}
Re = 15	6.712×10^{-3}	1.701×10^{-3}	4.213×10^{-4}	1.054×10^{-4}
Re = 20	9.561×10^{-3}	2.340×10^{-3}	5.953×10^{-4}	1.501×10^{-4}
Re = 25	1.354×10^{-2}	3.491×10^{-3}	8.835×10^{-4}	2.214×10^{-4}

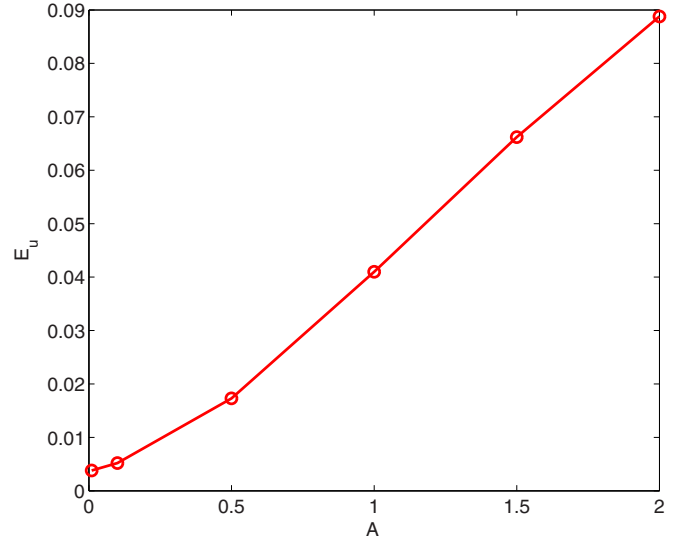
The results in Fig. 1 show that our numerical solutions are in good agreement with analytical solutions. Furthermore, the accuracies of the nonmodified (i.e., $A = 0$ in the modified LBGK model) and modified LBGK model are also tested on different grids. Toward that end, the following global relative error (GRE) of velocity is used:

$$E_u = \frac{\|\mathbf{u} - \mathbf{u}^*\|_2}{\|\mathbf{u}^*\|_2}, \quad (21)$$

where \mathbf{u} and \mathbf{u}^* are numerical and analytical solutions, respectively. The results can be seen in Tables I and II, and the relationship between GRE and lattice spacings is plotted in Fig. 2. The slopes of the fitting lines in Fig. 2(a) are about 1.9433, 1.9963, 1.9957, and 1.9767 for Re = 10, 15, 20, and 25, while the slopes in Fig. 2(b) are about 1.9863, 1.9906, 1.9958, and 1.999 for Re = 10, 15, 20, and 25. These results clearly demonstrate that, as with the nonmodified LBGK model, the modified LBGK model is of second-order accuracy in space. However, the results in Tables I and II show that when Re increases, GRE obtained by the modified LBGK model is larger than that derived by the nonmodified LBGK model. This situation may be caused by the large value of A . To confirm that, the influence of A on the accuracy of the modified LBGK model is investigated. Without loss of generality, the simulations are carried out at Re = 20, and the value of A is varied from 0 to 2. The results in Fig. 3 show that GRE increases with the increase of A . Therefore, to derive more accurate results, the value of A must be chosen carefully, and usually it should be less than 0.1.

B. Unsteady Womersley flow

In this subsection, the capacity of the modified LBGK model in studying unsteady flows is investigated through using unsteady Womersley flow, which is driven by a periodic pressure gradient. The geometry and velocity boundary conditions at the top and bottom walls of the problem are the same as the plane Poiseuille flow, while a periodic instead of a constant

FIG. 3. (Color online) GRE at different values of A .

pressure gradient is used,

$$\frac{\partial P}{\partial x} = G \cos(\omega t), \quad (22)$$

where G is the amplitude and $\omega = 2\pi/T$ is the frequency, with T representing the period of the pressure. Under the above conditions, we can obtain the analytical solution of the Womersley flow,

$$u(y, t) = \text{Re} \left[i \frac{G}{\omega} \left(1 - \frac{\cos[\lambda(2y/L - 1)]}{\cos \lambda} \right) e^{i\omega t} \right], \quad (23)$$

where $\lambda^2 = -i\alpha^2$, i is the complex unit, and $\alpha^2 = L^2\omega/4\nu$ is the Womersley number.

In our simulations, the velocity field is first initialized to be zero, and the simulation always begin with $10T$ steps to reach the convergence criterion,

$$\sum_i \frac{|\mathbf{u}(\mathbf{x}_i, t + T) - \mathbf{u}(\mathbf{x}_i, t)|}{|\mathbf{u}(\mathbf{x}_i, t + T)|} \leq 10^{-9}. \quad (24)$$

For the cases of $\alpha = 2.99$, 4.22, and 7.49, a 32×64 grid is used, while for a higher Womersley number of 11.85, a much finer grid (64×128) is adopted to accurately capture the variation of velocity at a pressure gradient with a high frequency. As can be seen from Fig. 4, the numerical results agree well with analytical solutions.

Next, we also test the accuracy of the modified LBGK model in simulating unsteady Womersley flow through measuring GRE at different lattice spacings, and we present a

TABLE II. GRE by the modified LBGK model with different Re numbers and different lattice spacings.

Re	E_u			
	$\delta x = 1/8$	$\delta x = 1/16$	$\delta x = 1/32$	$\delta x = 1/64$
Re = 10, $A = 0.02$	3.589×10^{-3}	9.328×10^{-4}	2.381×10^{-4}	6.022×10^{-5}
Re = 15, $A = 0.04$	7.289×10^{-3}	1.881×10^{-3}	4.813×10^{-4}	1.219×10^{-4}
Re = 20, $A = 0.06$	1.332×10^{-2}	3.354×10^{-3}	8.434×10^{-4}	2.118×10^{-4}
Re = 25, $A = 0.08$	2.047×10^{-2}	5.110×10^{-3}	1.280×10^{-3}	3.212×10^{-4}

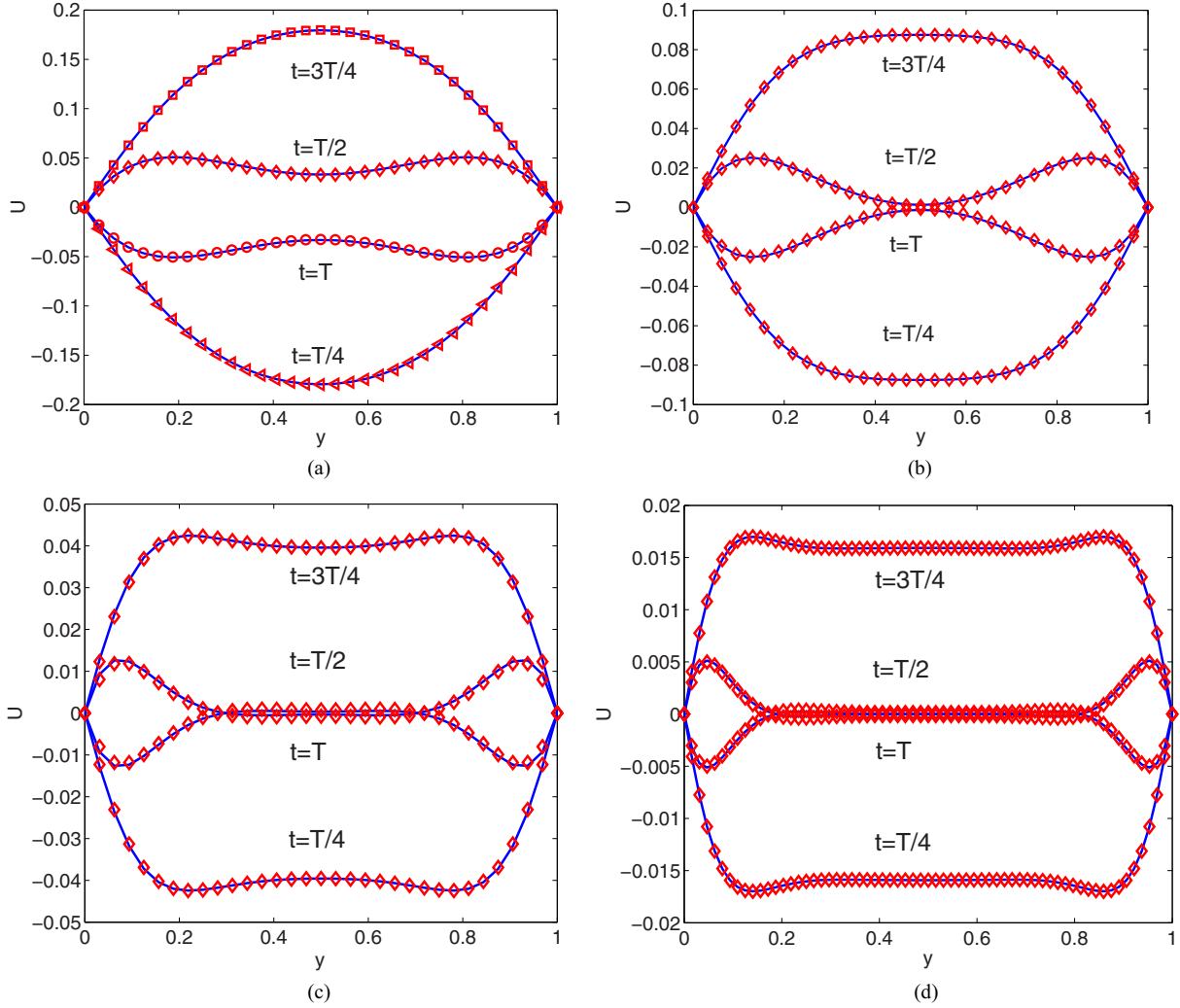


FIG. 4. (Color online) Comparisons between numerical results and analytical solutions at different time and Womersley numbers: (a) $\alpha = 2.99$, (b) $\alpha = 4.22$, (c) $\alpha = 7.49$, (d) $\alpha = 11.85$. Solid line: analytical solutions; symbols: numerical solutions.

comparison of the nonmodified and modified LBGK models at $t = T/4$ and $t = T$ in Tables III–VI. In addition, to see the convergence rates of the nonmodified and modified LBGK models more clearly, we also plot GRE at different lattice spacings and Womersley numbers in Figs. 5 and 6, and we found that the slopes of the fitting lines are in the range of [1.95, 2.0], which indicates that both the nonmodified and modified LBGK models have a second-order convergence rate in space. In addition, to validate that the modified LBGK model can still reduce the compressibility effect when simulating incompressible fluid flows, we still study the unsteady Womersley flow ($\alpha = 2.99$) by the modified LBGK model and compare the results with other models in Table VII. Here, Re is defined as the same as that in the Poiseuille flow. From Table VII, it is clear that, as the pressure drop increases, GRE obtained by the modified model or the D2G9 model at $t = T$ has no apparent difference, while GRE derived by the standard D2Q9 model increases rapidly due to the compressibility effect. It is thus demonstrated that the compressibility effect can also be eliminated by the modified model, as the D2G9 model does.

C. Natural convection in a square cavity

To further investigate the stability of the modified LBGK model, the natural convection in a square cavity is also considered. The schematic of the problem is shown in Fig. 7, where the horizontal walls are insulated while the two side walls are maintained at different temperatures T_h and T_c ($T_h > T_c$), respectively. The main dimensionless parameters of this problem are Pr and Ra , which are defined as $Pr = \nu/D = 0.71$, $Ra = g\beta\Delta TH^3/(\nu D)$, where β is the thermal expansion, $\Delta T = T_h - T_c$ is the temperature difference between the two side walls, and H is the height of the cavity. Under the Boussinesq approximation, all fluid properties are considered as constant except density, which is assumed to be a linear function of temperature in the buoyancy term.

For $10^3 \leq Ra \leq 10^6$, the natural convection is a laminar flow, and a 256×256 mesh grid is used. The streamlines and isotherms are presented in Figs. 8 and 9. As seen from these figures, there is only a vortex in the middle region of the cavity when Ra is small, and while the heat transfer is dominated by heat conduction, the isotherms are almost parallel to the vertical direction. However, with the increase

TABLE III. GRE by the nonmodified LBGK model with different Womersley numbers and lattice spacings at $t = T/4$.

Womersley number	E_u			
	$\delta x = 1/16$	$\delta x = 1/32$	$\delta x = 1/64$	$\delta x = 1/128$
$\alpha = 2.99$	5.831×10^{-3}	1.441×10^{-3}	3.726×10^{-4}	9.215×10^{-5}
$\alpha = 4.22$	9.271×10^{-3}	2.140×10^{-3}	5.442×10^{-4}	1.412×10^{-4}
$\alpha = 7.49$	1.532×10^{-2}	3.747×10^{-3}	9.425×10^{-4}	2.502×10^{-4}
$\alpha = 11.9$	1.923×10^{-2}	4.686×10^{-3}	1.263×10^{-3}	3.263×10^{-4}

TABLE IV. GRE by the nonmodified LBGK model with different Womersley numbers and lattice spacings at $t = T$.

Womersley number	E_u			
	$\delta x = 1/16$	$\delta x = 1/32$	$\delta x = 1/64$	$\delta x = 1/128$
$\alpha = 2.99$	9.206×10^{-3}	2.471×10^{-3}	5.836×10^{-4}	1.542×10^{-4}
$\alpha = 4.22$	1.743×10^{-2}	4.371×10^{-3}	1.115×10^{-3}	2.732×10^{-4}
$\alpha = 7.49$	2.415×10^{-2}	6.357×10^{-3}	1.716×10^{-3}	4.511×10^{-4}
$\alpha = 11.9$	3.420×10^{-2}	8.931×10^{-3}	2.473×10^{-3}	6.541×10^{-4}

TABLE V. GRE by the modified LBGK model with different Womersley numbers and lattice spacings at $t = T/4$.

Womersley number	E_u			
	$\delta x = 1/16$	$\delta x = 1/32$	$\delta x = 1/64$	$\delta x = 1/128$
$\alpha = 2.99$	5.527×10^{-3}	1.425×10^{-3}	3.715×10^{-4}	9.366×10^{-5}
$\alpha = 4.22$	9.854×10^{-3}	2.547×10^{-3}	6.376×10^{-4}	1.527×10^{-4}
$\alpha = 7.49$	1.625×10^{-2}	4.326×10^{-3}	1.083×10^{-3}	2.813×10^{-4}
$\alpha = 11.9$	2.221×10^{-2}	5.746×10^{-3}	1.473×10^{-3}	3.782×10^{-4}

TABLE VI. GRE by the modified LBGK model with different Womersley numbers and lattice spacings at $t = T$.

Womersley number	E_u			
	$\delta x = 1/16$	$\delta x = 1/32$	$\delta x = 1/64$	$\delta x = 1/128$
$\alpha = 2.99$	9.136×10^{-3}	2.364×10^{-3}	6.153×10^{-4}	1.584×10^{-4}
$\alpha = 4.22$	1.763×10^{-2}	4.726×10^{-3}	1.256×10^{-3}	3.257×10^{-4}
$\alpha = 7.49$	2.347×10^{-2}	6.315×10^{-3}	1.674×10^{-3}	4.458×10^{-4}
$\alpha = 11.9$	3.523×10^{-2}	9.264×10^{-3}	2.486×10^{-3}	6.535×10^{-4}

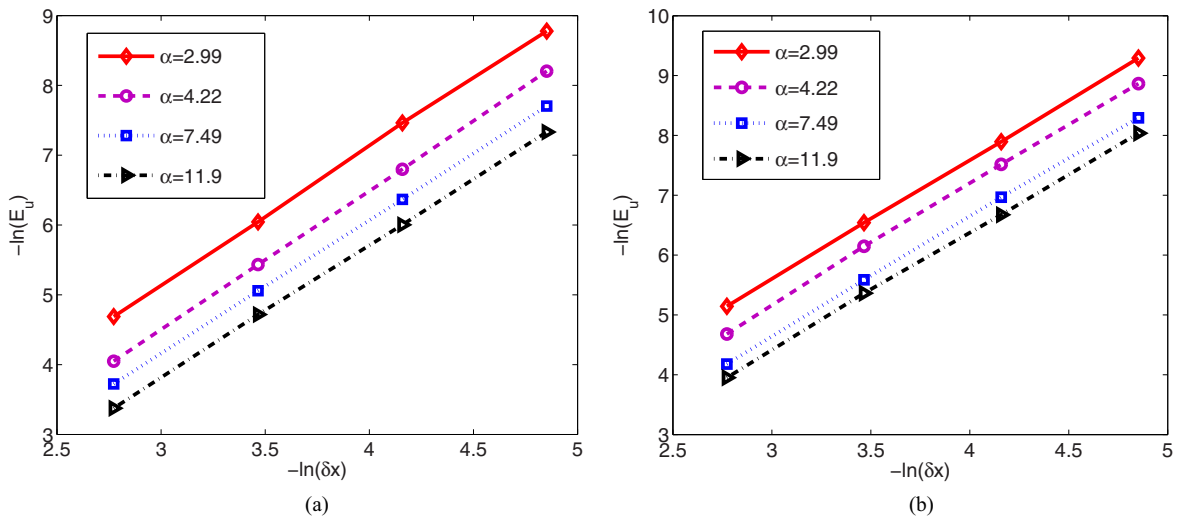


FIG. 5. (Color online) GRE obtained by the nonmodified LBGK model at different lattice spacings and Womersley numbers: (a) $t = T$, (b) $t = T/4$.

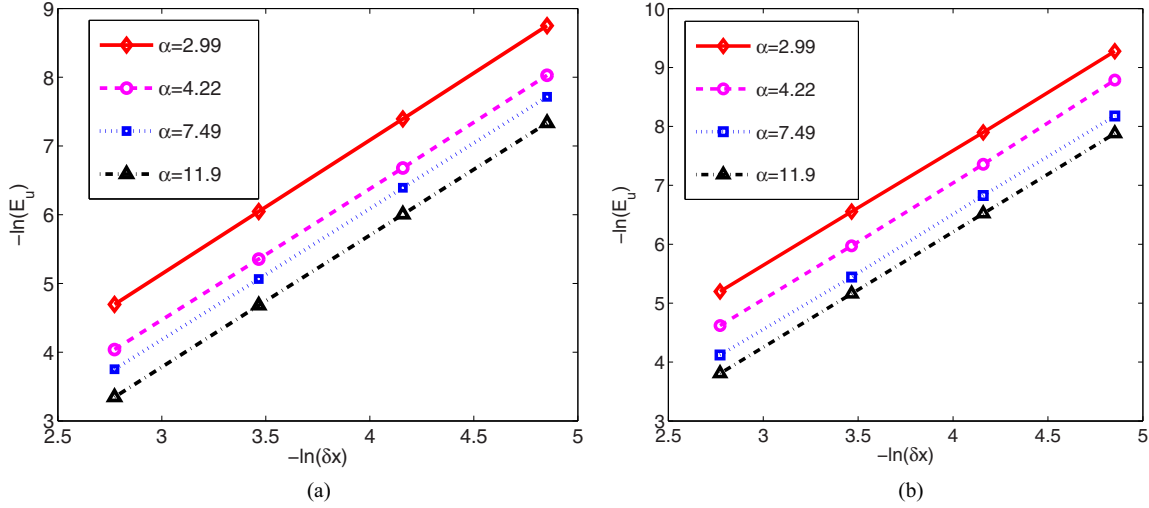


FIG. 6. (Color online) GRE obtained by the modified LBGK model at different lattice spacings and Womersley numbers: (a) $t = T$, (b) $t = T/4$.

of Ra , the convection effect becomes more significant. The central vortex tends to become elliptic at $Ra = 10^4$, and it breaks up into two vortices at $Ra = 10^5$. When Ra is increased further to 10^6 , the two vortices move toward the two side walls, and a third vortex appears in the core of the cavity. In addition, due to the convection effect, the isotherms become horizontal in the center of the cavity, and they are only vertical in the thin boundary layers near the two side walls. To check the temperature variation more clearly, we present the temperature distributions at the midheight of the cavity in Fig. 10, where Ra is varied from 10^3 to 10^6 . As shown in this figure, a linear distribution of temperature can be observed for the case of $Ra = 10^3$, which is consistent with the above discussion. However, the temperature profile becomes horizontal in the center of the cavity with the increase of Ra , and a much steeper temperature gradient appears near the vertical walls. We note that these results are qualitatively in line with the results reported in some published literature [17,33,34].

To give a quantitative analysis, the maximum horizontal velocity component at the midwidth (u_{max}), the maximum vertical velocity component at the midheight (v_{max}), the maximum Nusselt number (Nu_{max}), and the averaged Nusselt number (Nu_{av}) along the hot wall are computed and compared with some previous benchmark results. Here the averaged Nusselt number Nu_{av} is defined as

$$Nu_{av} = -\frac{1}{T_h - T_c} \int_0^{L_y} \left(\frac{\partial T}{\partial x} \right)_{wall} dy, \quad (25)$$

TABLE VII. GRE as a function of pressure drop in Womersley flow.

ΔP	Re	u_{max}	Ma	E_u		
				Modified model	D2G9 model	D2Q9 model
0.01	0.5	0.0177	0.0099	0.0025	0.0024	0.0024
0.02	1.0	0.0354	0.0199	0.0025	0.0024	0.0030
0.05	2.5	0.0884	0.0496	0.0025	0.0025	0.0075
0.1	5.0	0.1768	0.0992	0.0025	0.0025	0.0156
0.2	10.0	0.3536	0.1985	0.0025	0.0025	0.0232

where L_y is the height of the hot wall. We present the quantitative comparison between present results and some published results in Table VIII, and we find that the relative errors, compared with the published results, are less than 0.41%, 0.83%, 1.52%, and 0.56% for u_{max} , v_{max} , Nu_{max} , and Nu_{av} , which demonstrate that the numerical results are in good agreement with the previous work.

The above simulations of the laminar flow are validations of the modified LBGK model. To prove that the stability of the LBGK model has been improved, the natural convection flows with high Ra numbers ($10^7 \leq Ra \leq 10^{12}$) are studied. In the following simulations, the dimensionless relaxation factors τ and τ_ϕ are set as $\tau = \tau_\phi = 0.6$ and the parameters A and B are smaller than 0.1. The instantaneous streamlines and isotherms of different Ra numbers are plotted in Figs. 11 and 12. From these figures, one can find that for $10^7 \leq Ra \leq 10^8$, the vortices are moving close to the boundary layer and the center vortex becomes narrow. The isotherms are almost horizontal at the

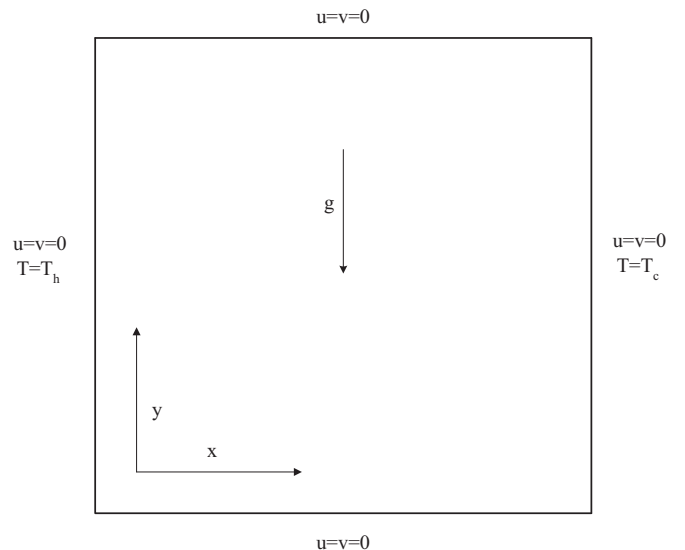


FIG. 7. Schematic diagram of the natural convection.

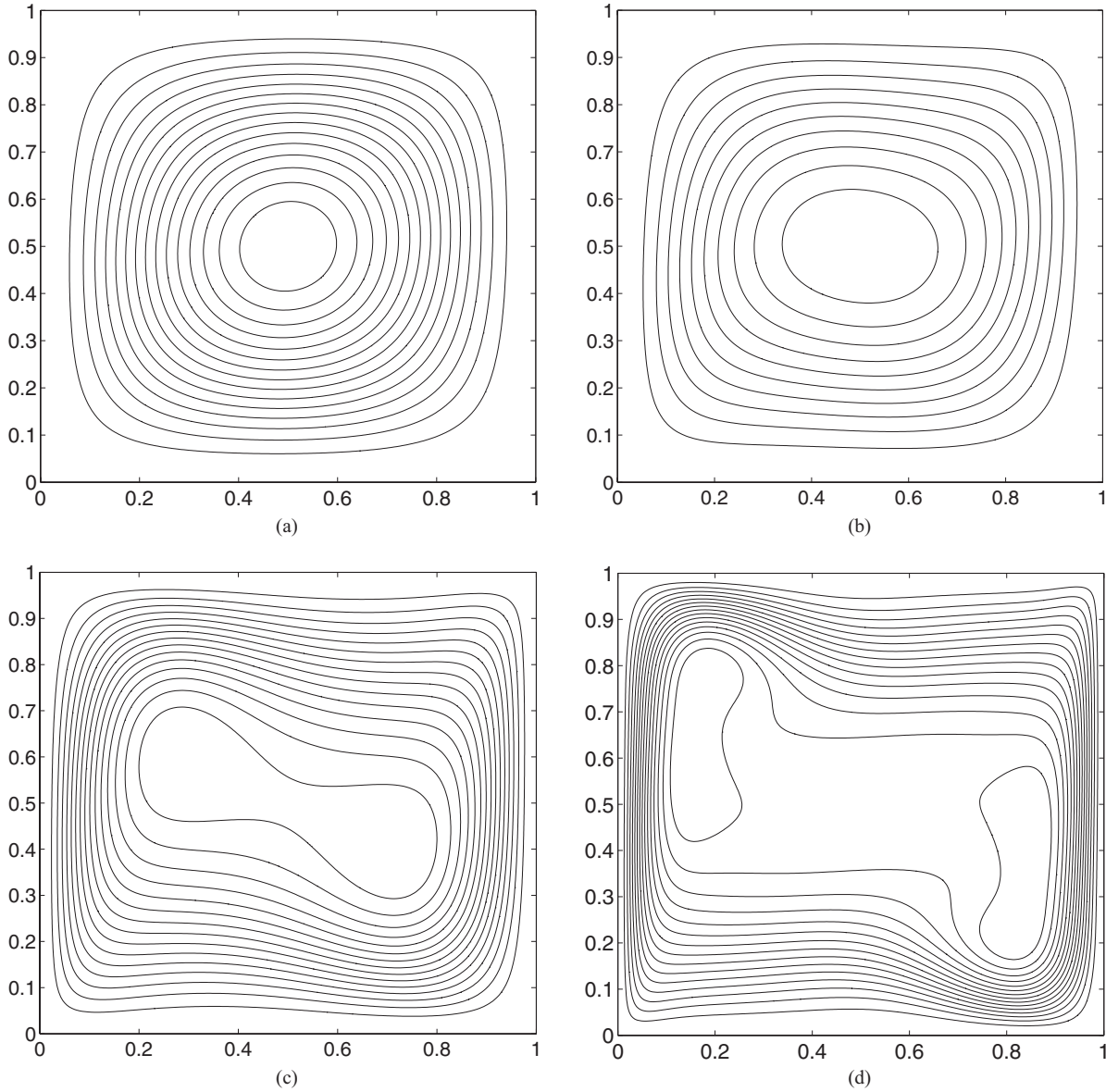


FIG. 8. Streamlines of the natural convection: (a) $Ra = 10^3$, (b) $Ra = 10^4$, (c) $Ra = 10^5$, (d) $Ra = 10^6$.

center of the cavity and become more and more dense near the two side walls. However, with the increase of Ra ($10^9 \leq Ra \leq 10^{12}$), the fluid flow becomes turbulent, and the streamlines in the whole region become very irregular and chaotic, which also cause the isotherms to become irregular, especially at the upper-left and bottom-right corners of the cavity. In addition, we also consider the variation of time-averaged temperature along the midheight of the cavity, and we present the results in Fig. 13. As seen from this figure, with the exception of the region near the walls, the temperature is almost constant, while the temperature distribution near the two side walls becomes much steeper for a larger Ra [see Fig. 13(b)]. Furthermore, we also conduct a comparison between the present results and those reported in the previous work in Fig. 14. For the cases of $Ra = 10^7$ and 10^8 , the temperature distributions agree well with those given by Dixit *et al.* [19], while for the cases of $Ra = 10^9$ and 10^{10} , the present results agree well with the data presented by Zhuo *et al.* [20], but they differ slightly with the results

reported in Ref. [19]. Furthermore, to illustrate the temperature fluctuations near the wall, the time-averaged Nu along the hot wall for different Ra numbers is depicted in Fig. 15. It can be observed that the maximum value of the heat flux is always at the very beginning of the vertical boundary layer where the mean temperature gradient is high due to the small thickness of the developing laminar boundary layer. For higher Ra ($Ra \geq 10^{11}$), a local maximum can be clearly observed at $y = 0.6$ due to the chaotic regime of the high Ra flows. Increasing Ra leads to a more efficient heat exchange in the last downstream part of the vertical wall. Next, in order to examine the chaotic flow at high Ra , we also survey Nu_{av} as a function of time at $Ra = 10^{11}$ and 10^{12} . It is seen from Fig. 16 that Nu_{av} oscillates dramatically and the flow has become fully turbulent.

It is well known that, for $10^7 \leq Ra \leq 10^8$, the natural convection is in a transitional region, and it becomes turbulent when Ra is increased to 10^9 . However, there are few studies on the critical Ra at which the flow becomes unsteady, and

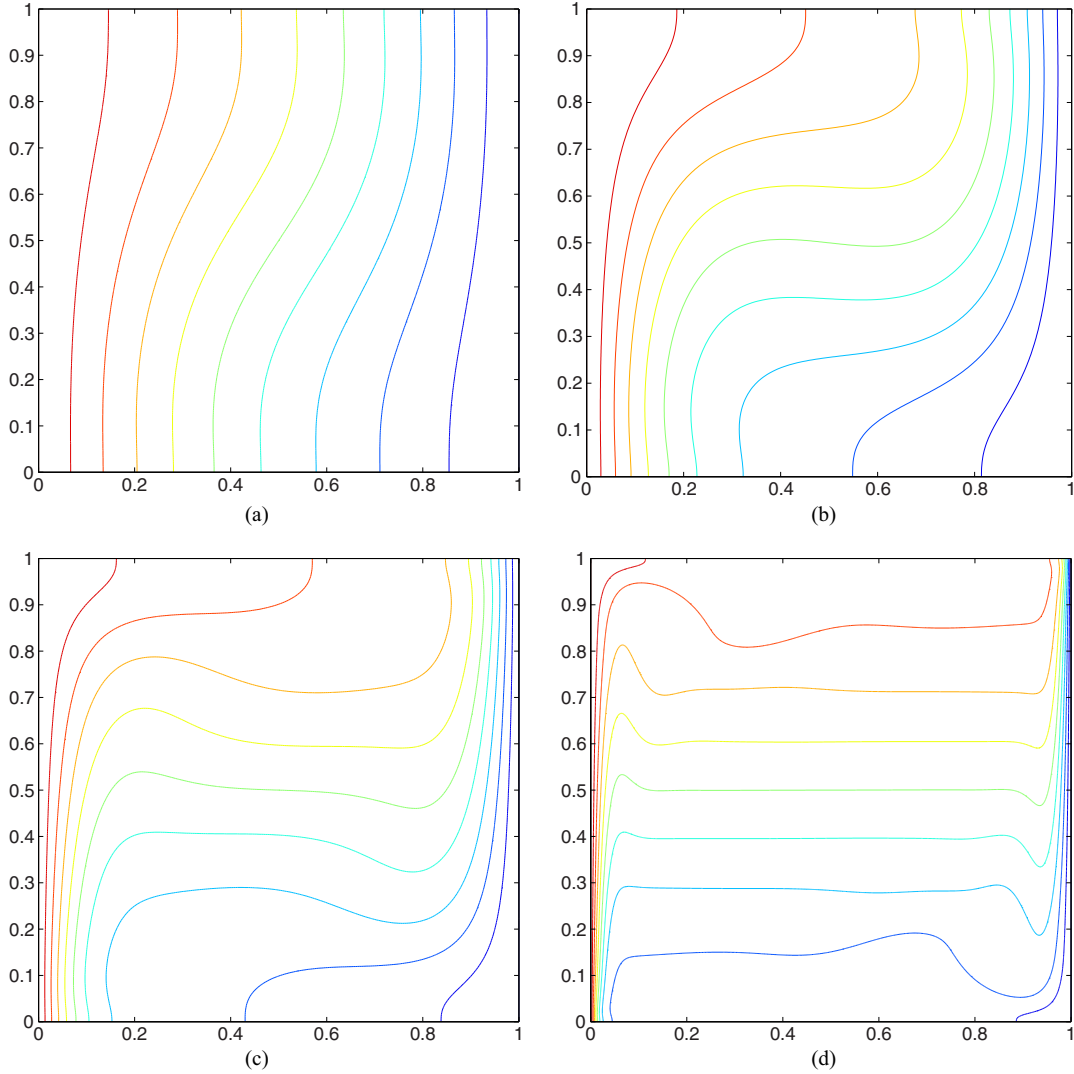


FIG. 9. (Color online) Isotherms of the natural convection: (a) $Ra = 10^3$, (b) $Ra = 10^4$, (c) $Ra = 10^5$, (d) $Ra = 10^6$.

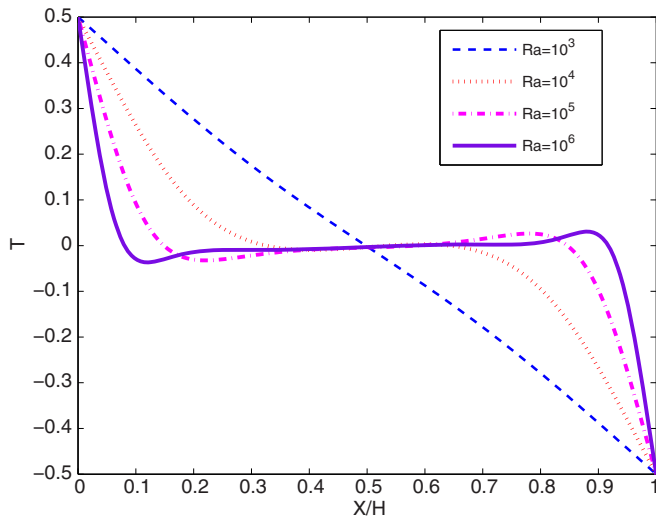


FIG. 10. (Color online) Temperature profiles at the midheight of the cavity from $Ra = 10^3$ to 10^6 .

TABLE VIII. Comparisons between the numerical results and the literature results ($Ra = 10^3-10^6$).

Ra		Guo <i>et al.</i> [17]	Hormann <i>et al.</i> [34]	Mezrhab <i>et al.</i> [33]	Our results
10^3	u_{max}	3.655	3.655	3.667	3.652
	v_{max}	3.703	3.703	3.714	3.703
	Nu_{max}	1.510	1.510		1.508
10^4	Nu_{av}	1.116	1.116	1.112	1.115
	u_{max}	16.194	16.180	16.202	16.171
	v_{max}	19.688	19.630	19.644	19.622
10^5	Nu_{max}	3.597	3.531		3.543
	Nu_{av}	2.244	2.244	2.241	2.247
	u_{max}	34.640	34.740	34.805	34.813
10^6	v_{max}	68.381	68.640	68.630	68.550
	Nu_{max}	7.823	7.730		7.762
	Nu_{av}	4.541	4.522	4.519	4.544
	u_{max}	64.313	64.837	64.793	64.675
	v_{max}	218.314	220.461	219.663	220.135
	Nu_{max}	17.709	17.536		17.640
	Nu_{av}	8.816	8.825	8.817	8.813

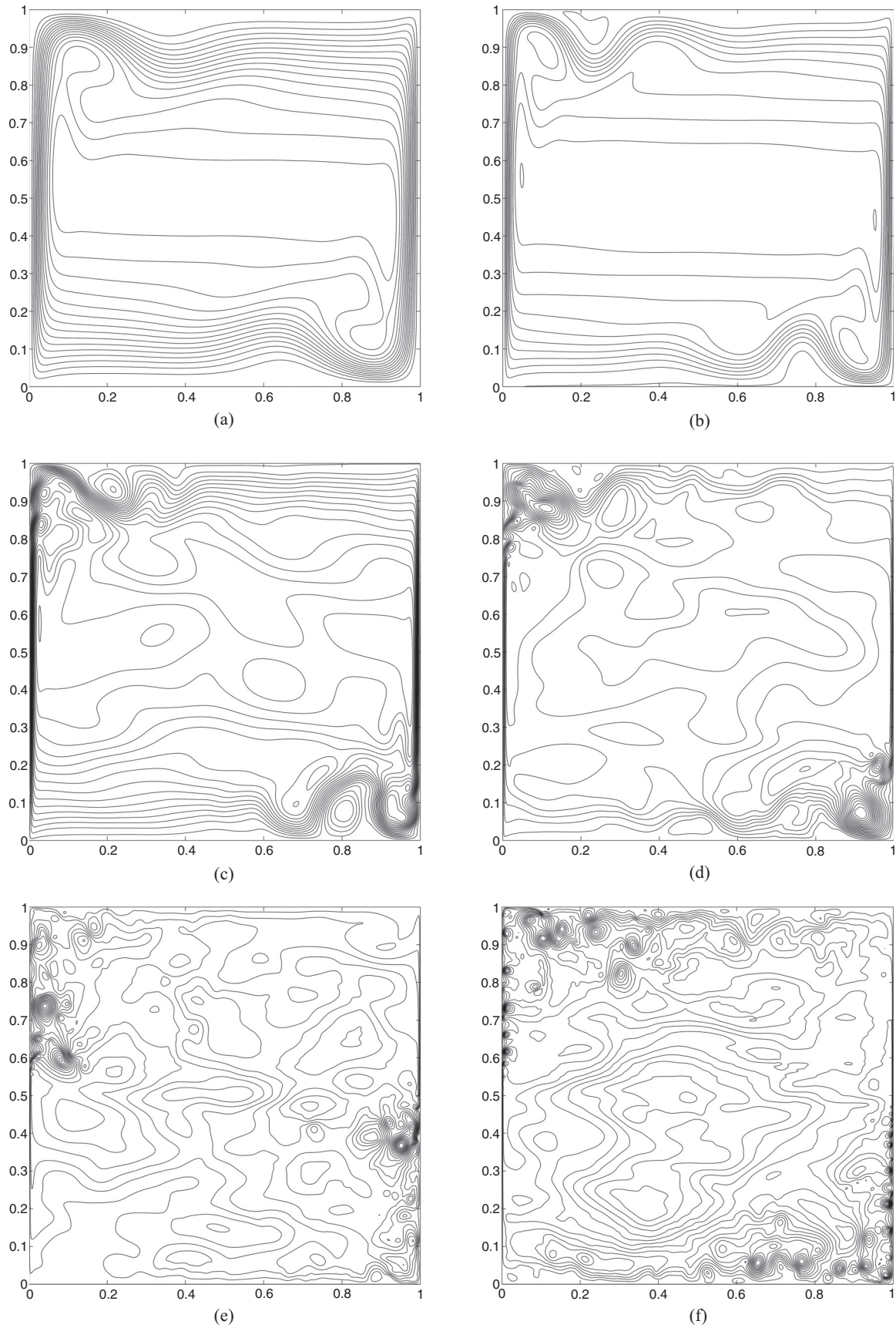


FIG. 11. The instantaneous streamlines of the natural convection: (a) $Ra = 10^7$, (b) $Ra = 10^8$, (c) $Ra = 10^9$, (d) $Ra = 10^{10}$, (e) $Ra = 10^{11}$, (f) $Ra = 10^{12}$.

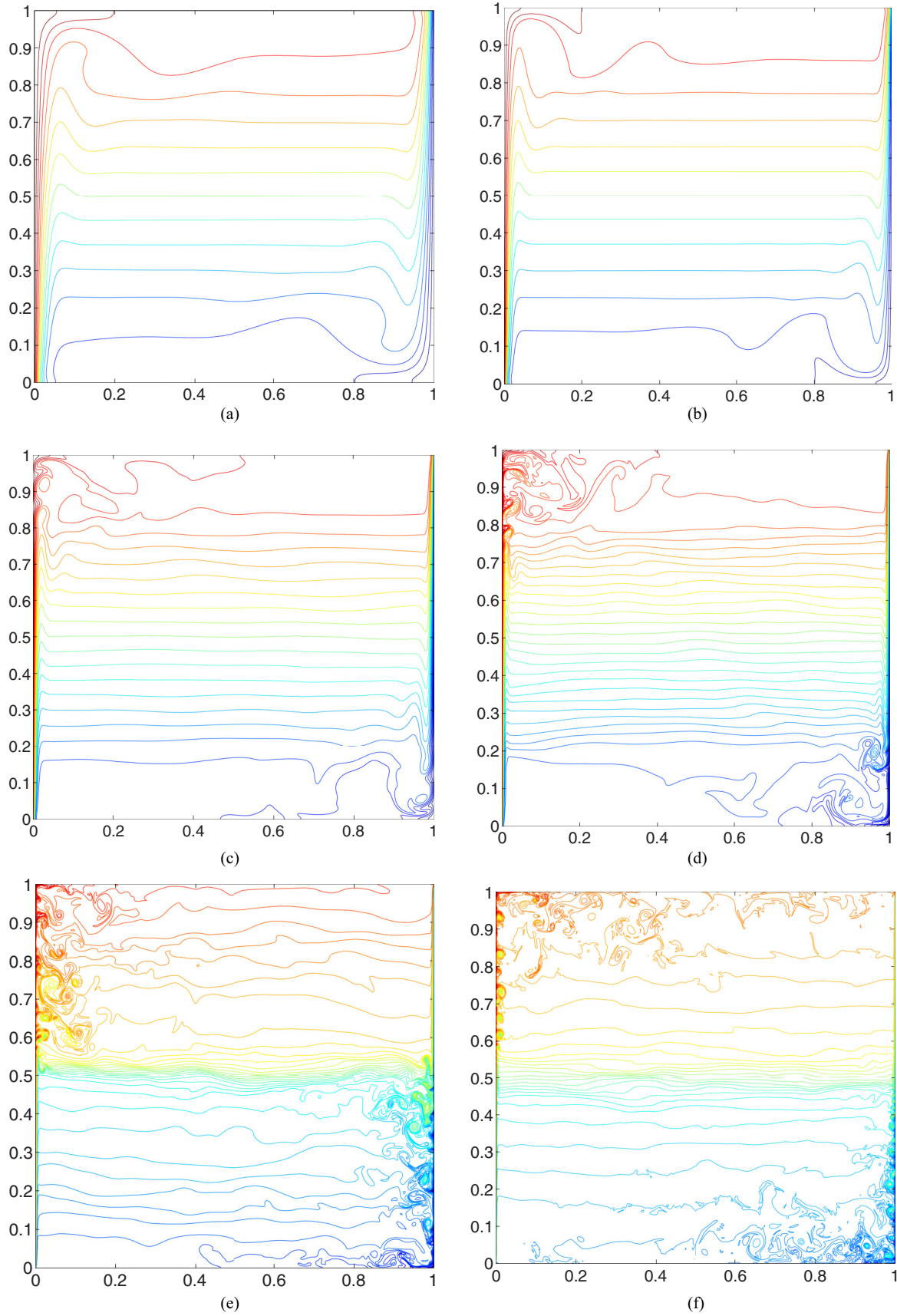


FIG. 12. (Color online) The instantaneous isotherms of the natural convection: (a) $Ra = 10^7$, (b) $Ra = 10^8$, (c) $Ra = 10^9$, (d) $Ra = 10^{10}$, (e) $Ra = 10^{11}$, (f) $Ra = 10^{12}$.

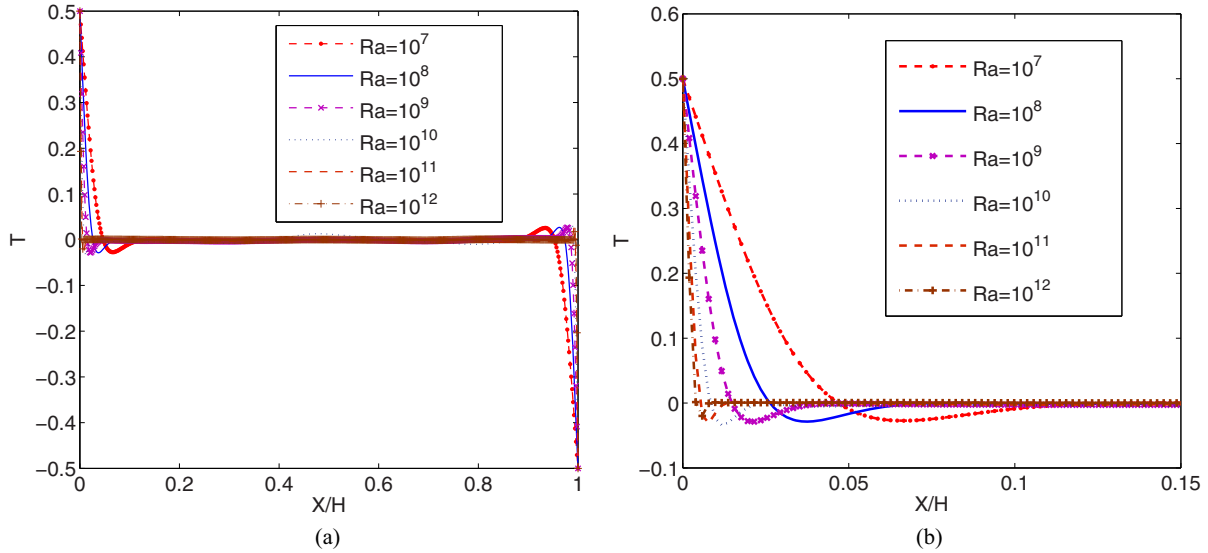


FIG. 13. (Color online) Temperature profiles (time-averaged) at the midheight of the cavity from $Ra = 10^7$ to 10^{12} : (a) the entire cavity, (b) enlarged view near the left wall.

this problem is worth investigating. To find the critical Ra , we consider the variations of Nu_{av} and u_{max} over time at different Ra numbers, and we show the results in Fig. 17. From this figure, we can see that for the case of $Ra = 1.8 \times 10^8$, the variation of u_{max} tends toward stability, and Nu_{av} oscillates a bit over time. As Ra further increases, the variations of both Nu_{av} and u_{max} become oscillating and are with increasing amplitude. From the above, we can conclude that the critical Ra is around 1.8×10^8 , above which the natural convection may become unsteady.

In addition, we also conduct a quantitative analysis on nature convection for $Ra = 10^7 - 10^{12}$, and we present the time-averaged results and the existing data in Table IX. It shows that the relative errors of the numerical results at the 512×512 and 1024×1024 grids are less than 6.94%,

4.73%, 6.05%, and 2.75% for u_{max} , v_{max} , Nu_{max} , and Nu_{av} , which demonstrate that the present results with the 512×512 grid are still accurate even at a very high Ra . Moreover, it can also be found that our results agree well with the previous work except for the data at $Ra = 10^{10}$ and 10^{12} by Markatos *et al.* [36]. This disagreement was interpreted by Barahos *et al.* [37] to indicate that the use of the standard $k-\epsilon$ model and logarithmic wall functions for the temperature and velocity in Ref. [36] lead to unusual overpredictions for Nu . To further validate our results, we also investigate the relationship between $Nu_{av}Ra^{-1/3}$ and Ra . As shown in Fig. 18, our results agree well with the solutions given by Barahos *et al.* [37] and Markatos *et al.* [36] when $Ra \leq 10^8$. However, when Ra becomes much larger ($Ra \geq 10^9$), our results start deviating from the solutions of Markatos *et al.* [36], but they agree well

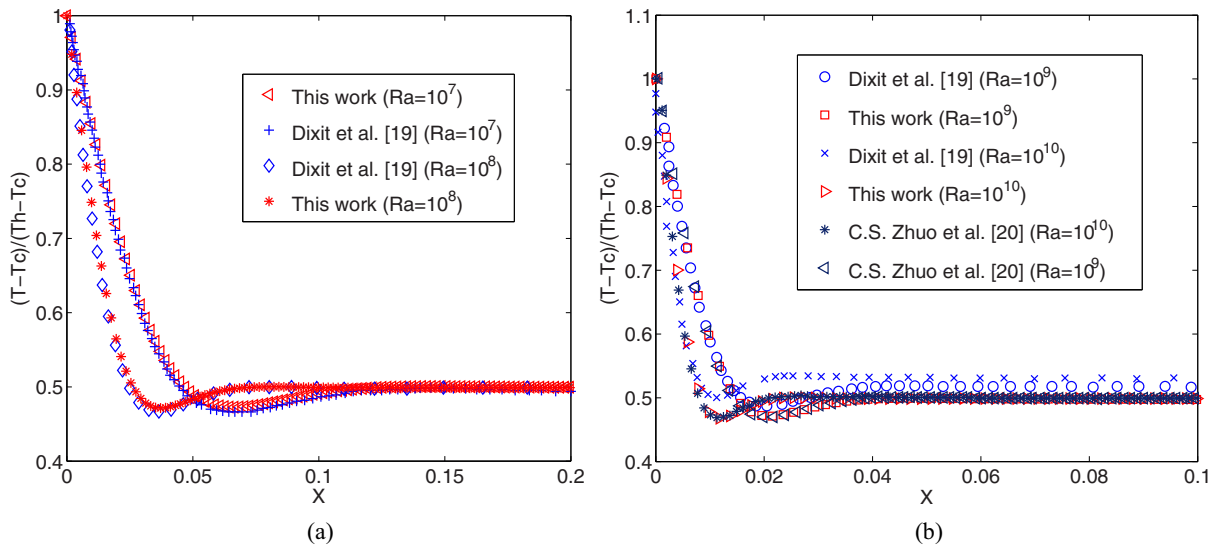


FIG. 14. (Color online) A comparison between present and previous works on temperature profiles (time-averaged) at the midheight of the cavity: (a) $Ra = 10^7 - 10^8$, (b) $Ra = 10^9 - 10^{10}$.

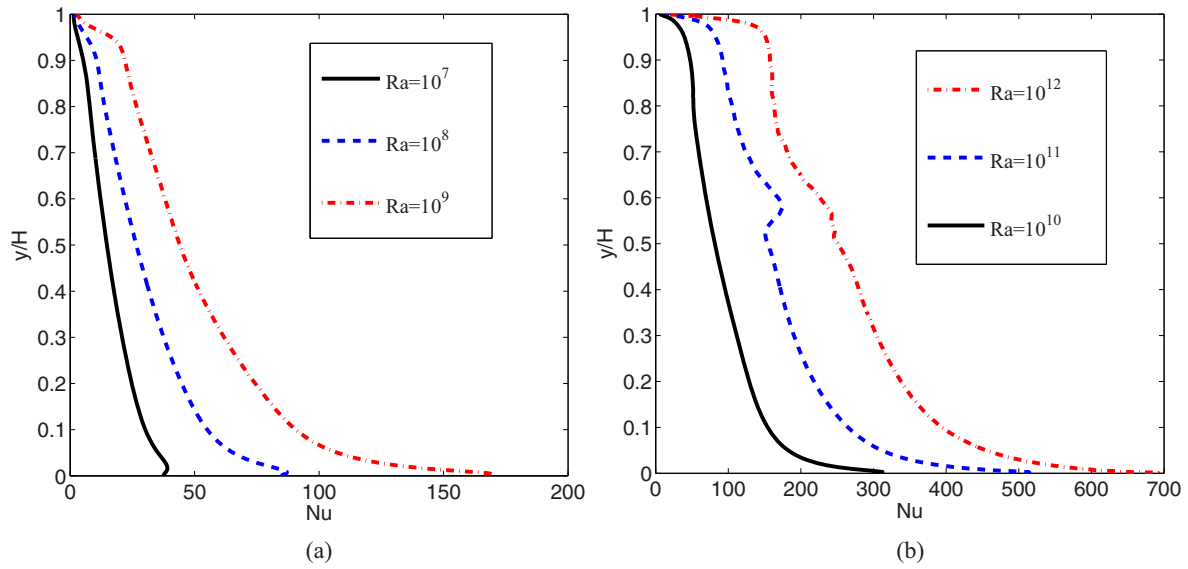


FIG. 15. (Color online) Time-averaged Nu along the hot wall: (a) $Ra = 10^7-10^9$, (b) $Ra = 10^{10}-10^{12}$.

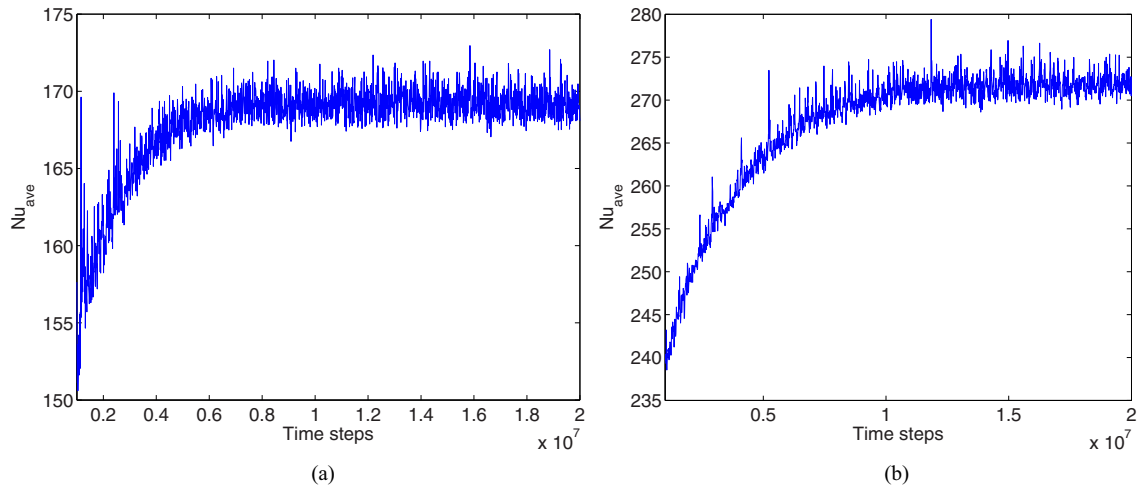


FIG. 16. (Color online) The variation of Nu_{ave} as a function of time: (a) $Ra = 10^{11}$, (b) $Ra = 10^{12}$.

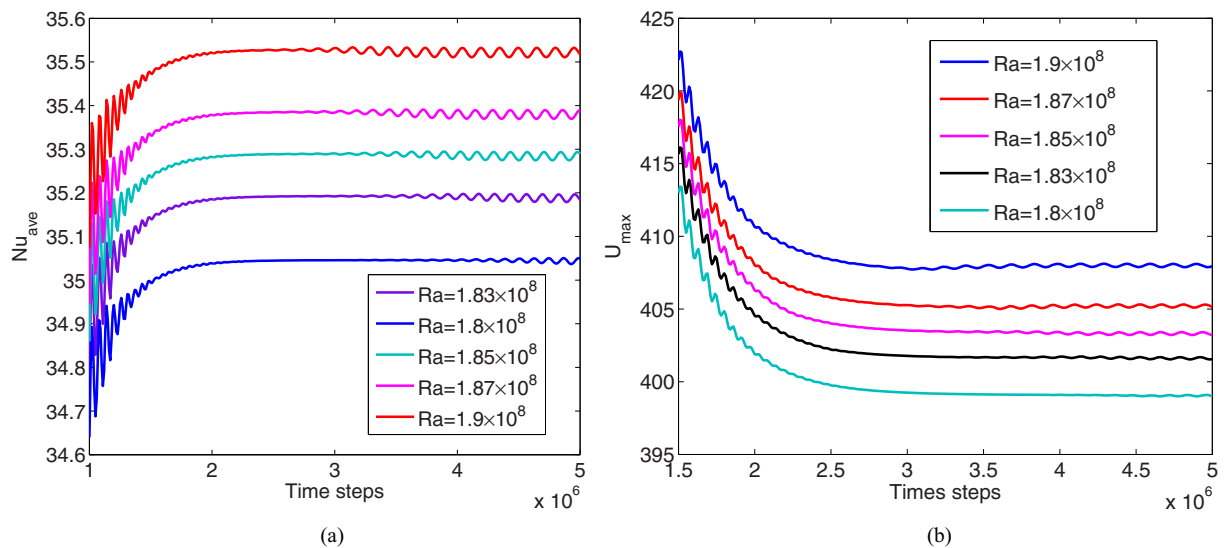


FIG. 17. (Color online) (a) The variation of Nu_{ave} as a function of time at different Ra numbers; (b) the variation of u_{max} as a function of time at different Ra numbers.

TABLE IX. Comparisons between the numerical results and the literature results ($Ra = 10^7-10^{12}$).

Ra		u_{max}	v_{max}	Nu_{max}	Nu_{av}
10^7	Le Quéré [35]	148.58	699.24		16.523
	Mezrhab <i>et al.</i> [33]	148.40	998.30		16.510
	Zhuo <i>et al.</i> [20]	148.32	695.50	38.269	16.512
	our results (512×512)	149.12	696.13	39.003	16.260
	our results (1024×1024)	151.19	698.22	39.078	16.393
10^8	Le Quéré [35]	321.88	2222.4		30.225
	Mezrhab <i>et al.</i> [33]	305.33	2169.6		30.033
	Zhuo <i>et al.</i> [20]	321.81	2207.9	78.762	30.195
	Markatos <i>et al.</i> [36]	514.30	1812	61.06	32.045
	our results (512×512)	329.06	2187.6	76.607	30.173
	our results (1024×1024)	337.83	2208.1	77.113	30.168
10^9	Zhuo <i>et al.</i> [20]	526.40	6991.7		54.510
	our results (512×512)	593.46	6703.2	168.55	53.931
	our results (1024×1024)	613.77	6810.4	176.87	54.336
10^{10}	Markatos <i>et al.</i> [36]	2323	16890	361.47	156.85
	Zhuo <i>et al.</i> [20]	1359	22135		98.171
	Barahos <i>et al.</i> [37]				97.60
	our results (512×512)	2476	19726	321.77	96.638
	our results (1024×1024)	2485	21651	341.81	98.013
10^{11}	Barahos <i>et al.</i> [37]				165.10
	Henkes <i>et al.</i> [38]				171.0
	our results (512×512)	3809	62072	525.85	167.89
	our results (1024×1024)	4093	65050	546.68	172.63
10^{12}	Markatos <i>et al.</i> [36]	12890	115600	2007.8	840.13
	our results (512×512)	19323	156707	682.53	267.13
	our results (1024×1024)	20427	164483	726.48	273.38

with the solutions of Barahos *et al.* [37]. These results also demonstrate that the solutions obtained by Markatos *et al.* yield unusual overpredictions for Nu.

Finally, to show the generality of the modification in the LBGK model, we also extend it to other models to study natural convection, and we present the results in Table X, where the results by LKS are also listed. As is seen from this table, the modified D2G9 model has the highest stability, while

the modified D2Q9 model, the He-Luo model, and LKS are divergent at high Ra.

IV. CONCLUSIONS

In this work, we showed how the stability of the LBGK model can be improved through a generalized modification. This modification is similar to LKS, but it has some important improvements. The first is that the law of mass conservation is satisfied in the modified LBGK model for incompressible Navier-Stokes equations. The second is that the correction term is put in the evolution equation rather than in the equilibrium distribution function, which is more reasonable. The third is that this modification is not limited to a specific LB model, and it can be extended to any other LB models. Finally, a local computational method for the gradient operator in the correction term is presented, which allows the whole collision

TABLE X. Comparison of different modified models for simulating natural convection.

Ra	Modified D2G9 model	Modified He-Luo model	Modified D2Q9 model	LKS
10^7	16.260	16.558	16.281	16.073
10^8	30.173	30.087	29.082	28.586
10^9	53.931	53.637	43.572	42.857
10^{10}	96.638	94.174	80.741	
10^{11}	167.89	153.22		
10^{12}	267.13			

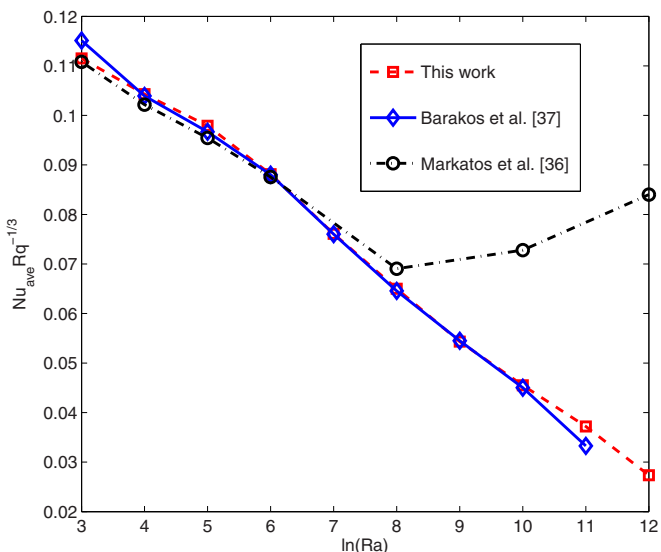


FIG. 18. (Color online) The variation of Nu_{av} as a function of Ra.

process to be implemented locally. For this reason, all of the above numerical simulations were performed on GPU, and a high computational efficiency can be obtained.

The numerical results of the steady Poiseuille flow and the unsteady Womersley flow show that, as with the other LBGK models, the modified LBGK model also has a second-order accuracy, while the compressibility effect can be eliminated, which is similar to the previous incompressible LBGK model. In addition, it is also found that the value of the tunable parameter must be chosen carefully, and usually it should be smaller than 0.1. To test the stability of the modified LBGK model, we have studied the natural convection in a square cavity, and we found that a very high Ra (Ra = 10¹²) can be achieved and the numerical results are in good agreement with some previous results. Furthermore, a comparison among different models shows that the modified D2G9 model is the most stable. At last, we also investigated the critical Ra of nature convection, and we found that it is about 1.8 × 10⁸. If Ra exceeds this value, the natural convection will become unsteady.

ACKNOWLEDGMENTS

We gratefully acknowledge Zhaoli Guo and Liang Wang for their helpful discussions during this work. This work is supported by the National Science Foundation of China (Grants No. 11272132, No. 51125024, No. 11302073, and No. 51306133) and the Fundamental Research Funds for the Central Universities (Grant No. 2014TS065).

APPENDIX: CHAPMAN-ENSKOG ANALYSIS ON THE MODIFIED LBGK MODEL

From Eqs. (4), (5), (6), (13), and (14), one can find that f_i , f_i^{eq} , S_i , g_i , g_i^{eq} , and \bar{S}_i satisfy

$$\sum_i f_i^{\text{eq}} = \sum_i f_i = \rho_0,$$

$$\sum_i \mathbf{c}_i f_i^{\text{eq}} = \sum_i \mathbf{c}_i f_i + \frac{1}{2} \Delta t \mathbf{a} = \mathbf{u},$$

$$\sum_i \mathbf{c}_i \mathbf{c}_i f_i^{\text{eq}} = p \mathbf{I} + \mathbf{u} \mathbf{u}, \quad (\text{A1a})$$

$$\sum_i S_i = 0, \quad \sum_i \mathbf{c}_i S_i = \left(1 - \frac{1}{2\tau}\right) \mathbf{a},$$

$$\sum_i \mathbf{c}_i \mathbf{c}_i S_i = \frac{c_s^2 A [\nabla \mathbf{u} + (\nabla \mathbf{u})^T]}{\tau} + \left(1 - \frac{1}{2\tau}\right) (\mathbf{a} \mathbf{u} + \mathbf{u} \mathbf{a}), \quad (\text{A1b})$$

$$\sum_i g_i^{\text{eq}} = \sum_i g_i = \phi, \quad \sum_i \mathbf{c}_i g_i^{\text{eq}} = \phi \mathbf{u},$$

$$\sum_i \mathbf{c}_i \mathbf{c}_i g_i^{\text{eq}} = c_s^2 \phi \mathbf{I} + \lambda \phi \mathbf{u} \mathbf{u}, \quad (\text{A1c})$$

$$\sum_i \bar{S}_i = 0, \quad \sum_i \mathbf{c}_i \bar{S}_i = \frac{c_s^2 B \nabla \phi}{\tau_\phi} + \left(1 - \frac{1}{2\tau_\phi}\right) \phi \mathbf{a},$$

$$\sum_i \mathbf{c}_i \mathbf{c}_i \bar{S}_i = 0. \quad (\text{A1d})$$

In the Chapman-Enskog analysis, the distribution function and the time and space derivatives can be expanded as

$$f_i = f_i^{(0)} + \varepsilon f_i^{(1)} + \varepsilon^2 f_i^{(2)} + \dots, \quad (\text{A2a})$$

$$g_i = g_i^{(0)} + \varepsilon g_i^{(1)} + \varepsilon^2 g_i^{(2)} + \dots, \quad (\text{A2b})$$

$$\frac{\partial}{\partial t} = \varepsilon \frac{\partial}{\partial t_1} + \varepsilon^2 \frac{\partial}{\partial t_2}, \quad \nabla = \varepsilon \nabla_1. \quad (\text{A2c})$$

Applying the Taylor series expansion to the evolution equations (3) and (11), we can get the following equations:

$$O(\varepsilon^0) f_i^{(0)} = f_i^{\text{eq}}, \quad (\text{A3a})$$

$$O(\varepsilon) D_{1i} f_i^{(0)} = -\frac{1}{\tau \Delta t} f_i^{(1)} + S_i^{(1)}, \quad (\text{A3b})$$

$$O(\varepsilon^2) \partial_{t_2} f_i^{(0)} + D_{1i} f_i^{(1)} + \frac{\Delta t}{2} D_{1i}^2 f_i^{(0)} = -\frac{1}{\tau \Delta t} f_i^{(2)}, \quad (\text{A3c})$$

$$O(\varepsilon^0) g_i^{(0)} = g_i^{\text{eq}}, \quad (\text{A4a})$$

$$O(\varepsilon^1) D_{1i} g_i^{(0)} = -\frac{1}{\tau_\phi \Delta t} g_i^{(1)} + \bar{S}_i^{(1)}, \quad (\text{A4b})$$

$$O(\varepsilon^2) \partial_{t_2} g_i^{(0)} + D_{1i} g_i^{(1)} + \frac{\Delta t}{2} D_{1i}^2 g_i^{(0)} = -\frac{1}{\tau_\phi \Delta t} g_i^{(2)}, \quad (\text{A4c})$$

where $D_{1i} = \partial/\partial t_1 + \mathbf{c}_i \cdot \nabla_1$.

Applying Eq. (A3b) to the left-hand side of Eq. (A3c), we can obtain

$$\begin{aligned} O(\varepsilon^2) \partial_{t_2} f_i^{(0)} + D_{1i} \left(1 - \frac{1}{2\tau}\right) f_i^{(1)} + \frac{\Delta t}{2} D_{1i} S_i^{(1)} \\ = -\frac{1}{\tau \Delta t} f_i^{(2)}. \end{aligned} \quad (\text{A5})$$

With the aid of Eqs. (A1a), (A2a), and (A3a), we have

$$\sum_i f_i^{(k)} = 0, \quad k > 0, \quad (\text{A6})$$

$$\sum_i \mathbf{c}_i f_i^{(1)} = -\frac{1}{2} \Delta t \mathbf{a}^{(1)}, \quad \sum_i \mathbf{c}_i f_i^{(k)} = 0, \quad k > 1. \quad (\text{A7})$$

From Eqs. (A1a), (A1b), (A6), and (A7), the moments of Eq. (A3b) lead to the first-order recovered equations in ε as

$$O(\varepsilon^1) \nabla_1 \cdot \mathbf{u} = 0, \quad (\text{A8a})$$

$$O(\varepsilon^1) \partial_{t_1} \mathbf{u} + \nabla_1 \cdot (p \mathbf{I} + \mathbf{u} \mathbf{u}) = \mathbf{a}^{(1)}. \quad (\text{A8b})$$

The moments of Eq. (A5) give the second-order recovered equations in ε^2 as

$$\begin{aligned} O(\varepsilon^2) \partial_{t_2} \mathbf{u} + \nabla_1 \cdot \left(1 - \frac{1}{2\tau}\right) \Pi^{(1)} \\ = -\frac{\Delta t}{2\tau} \nabla_1 \cdot \{c_s^2 A [\nabla_1 \mathbf{u} + (\nabla_1 \mathbf{u})^T]\} \\ - \frac{\Delta t}{2} \nabla_1 \cdot \left(1 - \frac{1}{2\tau}\right) (\mathbf{a}^{(1)} \mathbf{u} + \mathbf{u} \mathbf{a}^{(1)}), \end{aligned} \quad (\text{A9})$$

where $\Pi^{(1)} = \sum_i \mathbf{c}_i \mathbf{c}_i f_i^{(1)}$.

Utilizing Eq. (A3b), we get

$$\begin{aligned}\Pi^{(1)} &= \sum_i \mathbf{c}_i \mathbf{c}_i f_i^{(1)} = -\tau \Delta t \sum_i \mathbf{c}_i \mathbf{c}_i (D_{1i} f_i^{\text{eq}} - S_i^{(1)}) \\ &= -c_s^2 \Delta t (\tau - A) [\nabla_1 \mathbf{u} + (\nabla_1 \mathbf{u})^T] \\ &\quad - \frac{\Delta t}{2} (\mathbf{a}^{(1)} \mathbf{u} + \mathbf{u} \mathbf{a}^{(1)}) + O(\Delta t M a^2).\end{aligned}\quad (\text{A10})$$

Under the assumption of low Mach number, the term $O(\Delta t M a^2)$ can be neglected. Substituting Eq. (A10) into (A9) and combining the equations at t_1 and t_2 scales, we can get the incompressible Navier-Stokes equations,

$$\nabla \cdot \mathbf{u} = 0, \quad (\text{A11a})$$

$$\partial_t \mathbf{u} + \nabla \cdot \mathbf{u} \mathbf{u} = -\nabla p + \nabla \cdot \nu [\nabla \mathbf{u} + (\nabla \mathbf{u})^T] + \mathbf{a}, \quad (\text{A11b})$$

where $\nu = c_s^2 (\tau - \frac{1}{2} - A) \Delta t$.

In the same way, with the aid of Eq. (A4b), we can rewrite Eq. (A4c) as

$$\begin{aligned}O(\varepsilon^2) \partial_{t_2} g_i^{(0)} + D_{1i} \left(1 - \frac{1}{2\tau_\phi}\right) g_i^{(1)} + \frac{\Delta t}{2} D_{1i} \bar{S}_i^{(1)} \\ = -\frac{1}{\tau_\phi \Delta t} g_i^{(2)}.\end{aligned}\quad (\text{A12})$$

The moments of Eqs. (A4b) and (A12) can give the recovered equations in ε and ε^2 as

$$O(\varepsilon^1) \partial_{t_1} \phi + \nabla_1 \cdot \phi \mathbf{u} = 0, \quad (\text{A13a})$$

$$\begin{aligned}O(\varepsilon^2) \partial_{t_2} \phi + \nabla_1 \cdot \left(1 - \frac{1}{2\tau_\phi}\right) \sum_i \mathbf{c}_i g_i^{(1)} \\ + \frac{\Delta t}{2} \nabla_1 \cdot \left[\frac{c_s^2 B \nabla_1 \phi}{\tau_\phi} + \left(1 - \frac{1}{2\tau_\phi}\right) \mathbf{a}^{(1)} \right] = 0.\end{aligned}\quad (\text{A13b})$$

Based on Eq. (A4b), we have

$$\begin{aligned}\sum_i \mathbf{c}_i g_i^{(1)} &= -\tau_\phi \Delta t \sum_i \mathbf{c}_i (D_{1i} g_i^{\text{eq}} - \bar{S}_i^{(1)}) \\ &= -\tau_\phi \Delta t \left[\partial_{t_1} \phi \mathbf{u} + \lambda \nabla_1 \cdot (\phi \mathbf{u} \mathbf{u}) \right. \\ &\quad \left. + c_s^2 \left(1 - \frac{B}{\tau_\phi}\right) \nabla_1 \phi - \left(1 - \frac{1}{2\tau_\phi}\right) \phi \mathbf{a}^{(1)} \right] \\ &= c_s^2 (B - \tau_\phi) \Delta t \nabla_1 \phi - \frac{\Delta t}{2} \phi \mathbf{a}^{(1)} + O(\Delta t M a^2).\end{aligned}\quad (\text{A14})$$

Substituting Eq. (A14) into Eq. (A13b) and combining the equations at t_1 and t_2 scales, the convection-diffusion equation can also be recovered,

$$\frac{\partial \phi}{\partial t} + \nabla \cdot \mathbf{u} \phi = \nabla \cdot D \nabla \phi, \quad (\text{A15})$$

where $D = c_s^2 (\tau_\phi - 1/2 - B) \Delta t$.

-
- [1] R. Benzi, S. Succi, and M. Vergassola, *Phys. Rep.* **222**, 145 (1992).
- [2] S. Chen and G. D. Doolen, *Annu. Rev. Fluid Mech.* **30**, 329 (1998).
- [3] H. Chen, S. Kandasamy, S. Orszag, R. Shock, S. Succi, and V. Yakhot, *Science* **301**, 633 (2003).
- [4] U. Frisch, B. Hasslacher, and Y. Pomeau, *Phys. Rev. Lett.* **56**, 1505 (1986).
- [5] X. He and L. S. Luo, *Phys. Rev. E* **55**, R6333 (1997).
- [6] X. Shan and X. He, *Phys. Rev. Lett.* **80**, 65 (1998).
- [7] Z. Guo, B. Shi, and N. Wang, *J. Comput. Phys.* **165**, 288 (2000).
- [8] X. He and L. S. Luo, *J. Stat. Phys.* **88**, 927 (1997).
- [9] B. C. Shi and Z. L. Guo, *Phys. Rev. E* **79**, 016701 (2009).
- [10] M. R. Swift, E. Orlandini, W. R. Osborn, and J. M. Yeomans, *Phys. Rev. E* **54**, 5041 (1996).
- [11] I. Ginzburg, *Adv. Water Resour.* **28**, 1171 (2005).
- [12] X. He, N. Li, and B. Goldstein, *Mol. Simul.* **25**, 145 (2000).
- [13] S. G. Ayodele, F. Varnik, and D. Raabe, *Phys. Rev. E* **80**, 016304 (2009).
- [14] S. G. Ayodele, F. Varnik, and D. Raabe, *Phys. Rev. E* **83**, 016702 (2011).
- [15] S. G. Ayodele, D. Raabe, and F. Varnik, *Commun. Comput. Phys.* **13**, 741 (2013).
- [16] Z. H. Chai and T. S. Zhao, *Phys. Rev. E* **87**, 063309 (2013).
- [17] Z. Guo, B. Shi, and C. Zheng, *Int. J. Numer. Methods Fluids* **39**, 325 (2002).
- [18] B. C. Shi, N. Z. He, and N. C. Wang, *Prog. Comput. Fluid Dyn.* **5**, 50 (2005).
- [19] H. N. Dixit and V. Babu, *Int. J. Heat Mass Transfer* **49**, 727 (2006).
- [20] C. S. Zhuo and C. W. Zhong, *Int. J. Heat Fluid Flow* **42**, 10 (2013).
- [21] Y. H. Qian, *Int. J. Mod. Phys. C* **8**, 753 (1997).
- [22] G. R. McNamara, A. L. Garcia, and B. J. Alder, *J. Stat. Phys.* **81**, 395 (1995).
- [23] Z. L. Guo, C. G. Zheng, and T. S. Zhao, *J. Sci. Comput.* **16**, 569 (2001).
- [24] X. Q. Xiang, Z. H. Wang, and B. C. Shi, *Commun. Nonlin. Sci. Numer. Simul.* **17**, 2415 (2012).
- [25] T. Inamuro, *Philos. Trans. R. Soc. London, Ser. A* **360**, 477 (2002).
- [26] Y. Kataoka and T. Inamuro, *Philos. Trans. R. Soc. London, Ser. A* **369**, 2528 (2011).
- [27] M. Yoshino, Y. Hotta, T. Hirozane, and M. Endo, *J. Non-Newtonian Fluid Mech.* **147**, 69 (2007).
- [28] Y. Peng, C. Shu, Y. T. Chew, and T. Inamuro, *Phys. Rev. E* **69**, 016703 (2004).

- [29] Z. Guo, C. Zheng, and B. Shi, *Phys. Rev. E* **65**, 046308 (2002).
- [30] Z. Chai and T. S. Zhao, *Phys. Rev. E* **86**, 016705 (2012).
- [31] Y. H. Qian, D. d'Humières, and P. Lallemand, *Europhys. Lett.* **17**, 479 (1992).
- [32] Z. L. Guo, C. G. Zheng, and B. C. Shi, *Chin. Phys.* **11**, 366 (2002).
- [33] A. Mezrhab, M. A. Moussaoui, M. Jami, H. Naji, and M. Bouzidi, *Phys. Lett. A* **374**, 3499 (2010).
- [34] M. Horrmann and M. Peric, *Int. J. Numer. Methods Fluids* **11**, 189 (1990).
- [35] L. Le Quéré, *Comput. Fluids* **20**, 29 (1991).
- [36] N. C. Markatos and K. A. Pericleous, *Int. J. Heat Mass Transfer* **27**, 755 (1984).
- [37] G. Barakos and E. Mitsoulis, *Int. J. Numer. Methods Flow* **18**, 695 (1994).
- [38] R. A. W. M. Henkes, F. F. van der Vlugt, and C. J. Hoogendoorn, *Int. J. Heat Mass Transfer* **34**, 377 (1991).